Geomechanics and Engineering, *Vol. 28, No. 4 (2022) 335-346*
https://doi.org/10.12989/gae.2022.28.4.335

Analysis of the buckling failure of bedding slope based on monitoring data - a model test study

Qian Zhang[1], Jie Hu[*2,3], Yang Gao[1], Yanliang Du[1], Liping Li[3], Hongliang Liu[3] and Shangqu Sun[4]

[1]Key Laboratory of Structural Health Monitoring and Control, Shijiazhuang Tiedao University, Shijiazhuang, 050043, China
[2]School of Mechanical Engineering, Nanjing University of Science and Technology, Nanjing 210094, China
[3]Geotechnical and Structural Engineering Research Center, Shandong University, Jinan, 250061, China
[4]Shandong Provincial Key Laboratory of Civil Engineering Disaster Prevention and Mitigation,
Shandong University of Science and Technology, Qingdao 266590, Shandong, China

(Received February 19, 2020, Revised December 17, 2021, Accepted January 18, 2022)

Abstract. Buckling failure is a typical slope instability mode that should be paid more attention to. It is difficult to provide systematic guidance for the monitoring and management of such slopes due to unclear mechanism. Here we examine buckling failure as the potential instability mode for a slope above a railway tunnel in southwest China. A comprehensive model test system was developed that can be used to conduct buckling failure experiments. The displacement, stress, and strain of the slope were monitored to document the evolution of buckling failure during the experiment. Monitoring data reveal the deformation and stress characteristics of the slope with different slipping mass thicknesses and under different top loads. The test results show that the slipping mass is the main subject of the top load and is the key object of monitoring. Displacement and stress precede buckling failure, so maybe useful predictors of impending failure. However, the response of the stress variation is earlier than displacement variation during the failure process. It is also necessary to monitor the bedrock near the slip face because its stress evolution plays an important role in the early prediction of instability. The position near the slope foot is most prone to buckling failure, so it should be closely monitored.

Keywords: buckling failure; critical load; model test; monitoring data; slope

1. Introduction

With the rapid construction of infrastructure in China, numerous highways and railways are being built in western mountainous areas. These transportation routes include a large number of tunnels and bridges (Wang *et al.* 2019). The intensive tectonic movement formed western China's mountainous terrain, which is characterized by complex geological conditions and many high-steep slopes. The bridge and tunnel connection area are prone to landslide and rockfall disasters, which bring serious threats to the construction and operation of traffic engineering, as shown in Fig. 1. The prevention and control of collapse and landslide disasters have attracted the common concern of engineering and research staff (Wang *et al.* 2017, Hu *et al.* 2020, Kim *et al.* 2020).

Landslide disasters caused by instability of the bedding slope are most common in mountainous areas. In the traditional view, a steeply inclined bedding slope is stable. As the research on the instability mechanism of the slope deepens, more and more slip-buckling failures have been found in high-steep slopes, such as Jipazi landslide, Bawang Mountain landslide, and Dashankou landslide in southwestern China; typical buckling failure is shown in Fig. 2. Slip-buckling slope failure often occurs when the slope is intersected by a set of discontinuities approximately parallel to the surface forming a slab. Under the self-weight of rock slabs and other exterior factors including the pressure of deposit body, earthquake, and excavation unloading effect, the buckling failure is prone to occur on the slope (Cavers 1981, Park 2018). There has been limited research on the mechanism and stability control of slopes with buckling failure, and most studies adopted theoretical analyses and numerical simulations (Babanouri and Sarfarazi 2018, Yamaguchi *et al.* 2018). Current theory models treat the buckling of rock slabs as simplified beam or bar stability problems in elastic theory and use the principle of energy equilibrium (Cavers 1981). Analytical models formed from these theories provide a base for simple and quick assessment of slope stability. However, these simplified models do not capture the complexities of actual slope conditions, and may not be sufficiently accurate to address the slope stability problems. Additionally, most theories cannot correctly consider both the long-term process of gradual-continuous deformation and abrupt failure, and the critical points of the instability of a slope cannot be described well using theoretical analyses (Park 2018). Numerical methods can better solve the aforesaid disadvantages of most theoretical models. Some numerical methods have been adopted to simulate the buckling failure process of slopes, such as AFENA, Phase2, and UDEC (Pant and Adhikary 1999, Adhikary *et al.* 2001, Pereira and Lana 2013, Silva and Lana 2014). Numerical methods and theoretical analyses are more popular than

---

*Corresponding author, Ph.D.
E-mail: hjxz1996@163.com

ISSN: 2005-307X (Print), 2092-6219 (Online)


(a)

(b)

Fig. 1 Threats on traffic caused by rockfall and landslide; (a) landslide disaster and (b) rockfall disaster

model tests in the economy and convenience (Ning *et al*. 2015). However, because the models need to be simplified, they fail to fully describe the complex field geological conditions of a site. Geotechnical model tests can directly reflect the physical and mechanical phenomena of the system (Zhu *et al*. 2010, Zhang *et al*. 2019) and the failure of the rock mass can be directly observed. For the stability analysis of bedding slope, researchers have carried out large numbers of model tests and acquired useful data and test cases (Nakajima *et al*. 2019, Lin *et al*. 2015, Moradi *et al*. 2019). The focus of the present model tests includes ① Mechanism and starting criterion of landslide under the external factors, such as rainfall and earthquake; ② Progressive instability and failure regularity of slope; ③ Influence of excavation construction on slope stability; ④ Anti-slip mechanism of slope reinforcement measures. However, model tests and research on buckling failures of bedding slopes are not well documented in the literature. There are still some limits to our knowledge about the mechanism of slope buckling failure and the instability process.

In this paper, a combined model test system was developed to study the mechanism of slope buckling failure caused by exterior loading. The test design was based on a detailed geological investigation for an actual bedding slope, which is adjacent to a tunnel portal in southwestern China. Meanwhile, a module simulating rockfall was added to the model test system because the tunnel portal is also prone to rockfall disasters. The creative design can meet the needs of carrying out multiple experiments. While we focus on the mechanism of buckling failure, related and subsequent experiments will be conducted to study rockfall disasters. An artificial model slope was constructed emulating material of the actual slope lithology.

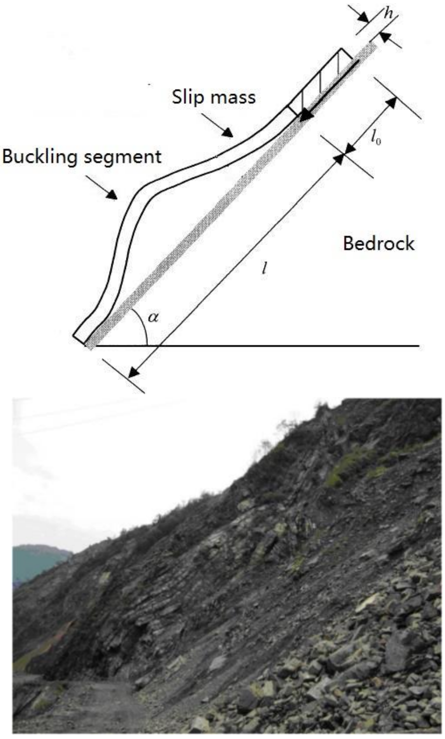

Fig. 2 Schematic of buckling slope failure and example of slope undergoing buckling failure in southwestern (Qi *et al*. 2015)

Experiments of different test sets were conducted on the test system, and multiple methods were used to measure the stress, displacement, and strain of the slope in the experiments. Variation regularities of displacement, stress, and strain of slope were analyzed to investigate the evolution of buckling failure and determine the critical loads that the slipping mass can bear with different thicknesses. The results clarify the mechanism of slope instability and provide an important reference for the construction, monitoring, and reinforcement of the actual slope.

2. Engineering background

The prototypical slope in this paper is adjacent to the portal of one railway tunnel, about 200 km north of Chengdu City in southwestern China (Fig. 3). The study area is located on the eastern edge of the Tibet plateau with mountain ranges in a north-south line. The terrain is incised intensely and precipitously. The tectonic formations are highly developed in this area and several orogenic episodes contributed to folding, faulting, metamorphism, and intrusion. This intense deformation resulted in complexly folded rock masses cut by north-south trending faults, which are associated with broad zones of weak materials and differential weathering. The layers mainly consist of phyllite belonging to the Zhuwo Formation (T3zh) that have undergone different degrees of weathering. The potential slipping mass on the slope is soft and moderately

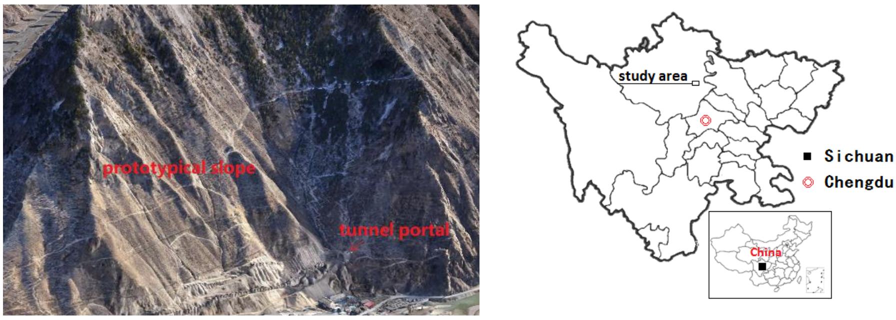

Fig. 3 The aerial image and location of prototypical slope

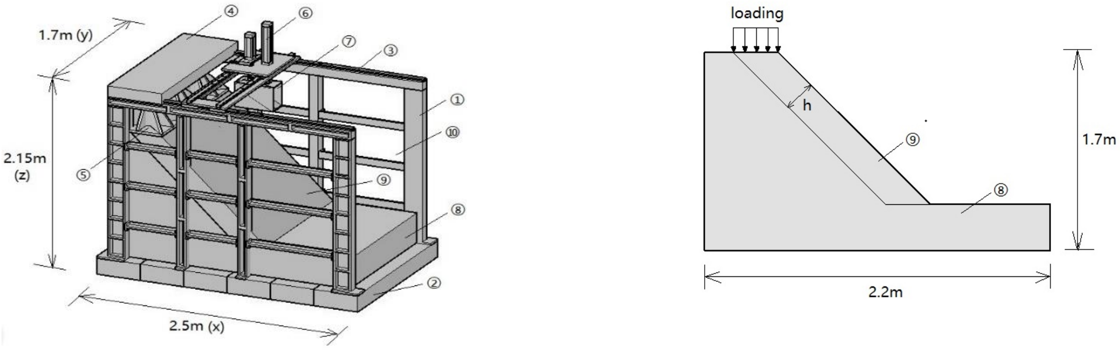

Fig. 4 Design drawing of the model test system: ① Steel frame; ② Base; ③ Slide track; ④ Anti-force device; ⑤ Jack; ⑥ Gas pressure cylinder; ⑦ Block release box; ⑧ Slope; ⑨ Slipping mass; ⑩ Toughened glass. The "h" means thickness of the slipping mass; and the "x", "y", "z" means the different axis

weathered, and the joint fracture is relatively developed. The bedrock of the slope is relatively hard and weakly weathered, and the integrity is better than the slipping mass. The slope angle is about 50° according to the aerial image in Fig. 3 and the geological investigation. In addition, rockfall events are common in this area because of weathering and the many unstable blocks that are perched on the hilltop along the slope, which also threatens the safety of tunnel construction.

3. Design of model test

3.1 Test apparatus

Experiments were carried out in the self-developed steel structure test bench (Hu *et al*. 2017). The steel frame of test devices in this system is 1.7 m in width, 2.2 m in height, and almost 2.5 m in length at the bottom boundary. The bench was composed of steel frames and high-strength bolts. Two pieces of high-strength tempered-glass were installed on both sides of an exterior steel frame so that the experiment was visible. In addition, steel frames were assembled and disassembled according to actual requirements. An anti-force device was mounted on the bench, with which the hydraulic cylinder can load on the slope. The size of the artificial slope is 2.2 m × 1.5 m × 1.8 m (length × width × height) and the slope angle is 50°. The composition of the rock-release device includes a release box with an adjustable inclined bottom, two types of gas pressure cylinder (one is for lifting and dropping the box, the other for controlling the inclination of the box bottom), and three sets of slide tracks to meet the requirement of simulating rockfall at any position. The release box can be moved along the slide tracks to realize position change in x or y-direction. Fig. 4 shows the design of model test devices.

3.2 Development of similar material

The ratio of the same physical quantity between prototype and model is called the similarity ratio (Zhang *et al*. 2016). The geomechanical model must satisfy the three similitude requirements of scale, loading, and material properties. Generally, the similarity constant for weight by volume, C_r, is set as 1, to equate the gravity field between the prototype and the model in a static test. If this condition is met, the conversion of the other parameters should be straightforward (Lin *et al*. 2014). In this study, the similarity ratio of geometry $C_l = 50$. The unit weight of the prototype is the same as that of the model, i.e. $C_r = 1$. Similarity ratios of other parameters can be deduced according to similarity theory as follows

$$C_\sigma = \frac{\sigma_p}{\sigma_m} = C_r C_l = 50;\ C_E = \frac{E_p}{E_m} = C_\sigma = 50;\ C_c = \frac{c_p}{c_m} = C_\sigma = 50$$

$$C_\varepsilon = \frac{\varepsilon_p}{\varepsilon_m} = \frac{\Delta l_p / l_p}{\Delta l_m / l_m} = 1;\ C_f = \frac{f_p}{f_m} = 1;\ C_\mu = \frac{\mu_p}{\mu_m} = 1$$

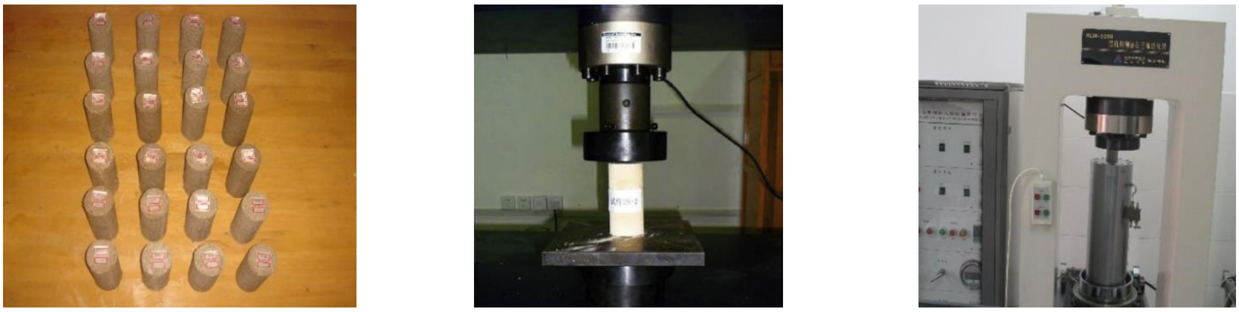
(a) (b) (c)

Fig. 5 Mechanical experiment on similar material specimens: (a) similar material specimens, (b) uniaxial compression test and (c) triaxial compression test

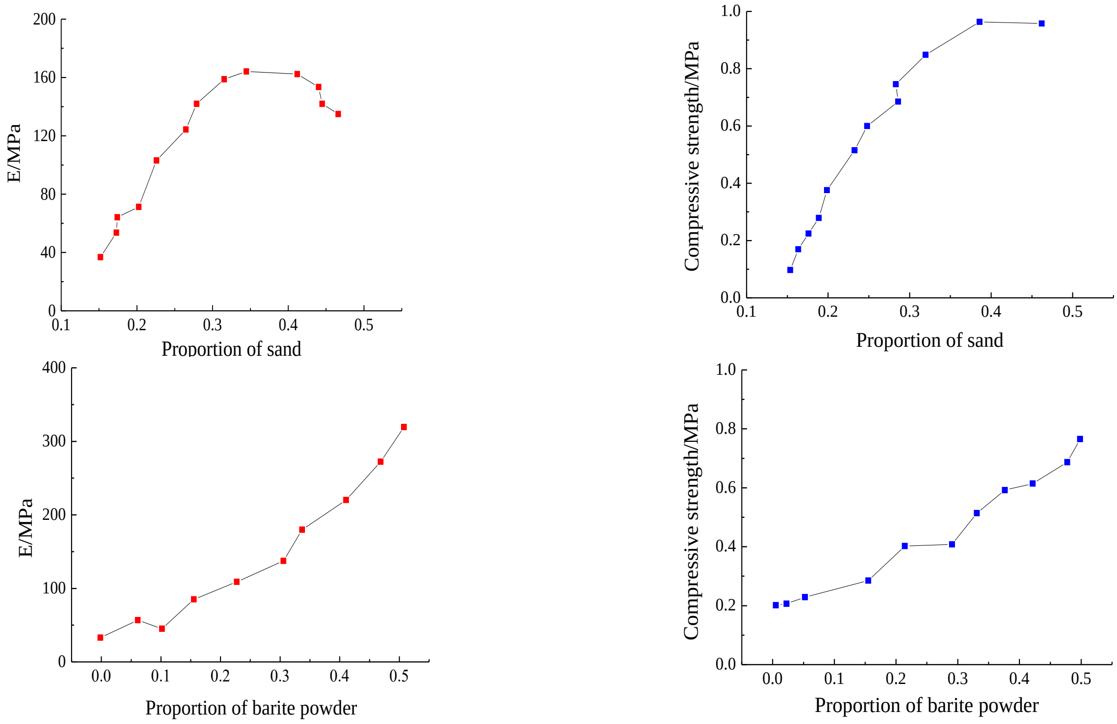

Fig. 6 Influence curves of mechanical parameters affected by the proportion (based on mass) of sand and barite powder

Where C_σ is similarity scale of stress, C_E is similarity scale of elastic modulus, C_c is similarity scale of cohesion, C_ε is similarity scale of strain, C_f is similarity scale of internal friction angle, and C_μ is similarity scale of Poisson's ratio. In the above equations, subscripts p and m denote the prototype and model respectively.

Owing to the differences in physico-mechanical properties between slipping mass and bedrock, we describe the use of materials to simulate the moderately weathered phyllite and weakly weathered phyllite. The similar material of slipping mass adopted the material developed by Hu *et al.* (2017), the composition includes sand, barite powder, silicone oil, vaseline, water, cement, and talc powder. The similar material used to simulate the bedrock was developed by changing the proportion of the material component based on a similar material simulating the slipping mass. Large numbers of tests were conducted to acquire the physico-mechanical parameters; the process was shown in Fig. 5. For each material, five specimens with the size of $\phi 50\times100$ mm were selected and five different confiningpressure σ_3 were applied around the specimens. Each conventional triaxial test can obtain a peak strength σ_1. And based on the values of σ_1 and σ_3 in the tests, the Mohr circles were drawn with the center of ($\sigma_1+\sigma_3$)/2 and the radius of ($\sigma_1-\sigma_3$)/2 in the coordinate system. The internal friction angle φ and cohesion c can be obtained by the fitted common tangent line of several Mohr circles (Li *et al.* 2021). Regarding the determination of compressive strength and elastic modulus, five specimens with the size of $\phi 50\times100$ mm were selected to conduct the uniaxial compression tests for each material, and the mean value of the test results was adopted. As for the tensile strength, Brazil split tests were conducted on the five specimens with the size of $\phi 50\times50$ mm for each material, and the mean value was also used. The test results indicate that the proportions of sand and barite powder influence the mechanical properties, as shown in Fig. 6. The physico-mechanical parameters of slipping mass, bedrock, and their corresponding similar materials are listed in Table 1, and

Table 1 Physico-mechanical parameters of slipping mass, bedrock and their corresponding similar materials

Material type	Unit weight (kN/m^3)	Elastic modulus (MPa)	Compressive strength (MPa)	Tensile strength (MPa)	Poisson ratio	Cohesion (MPa)	Internal friction angle (°)
Slipping mass	25.5	3.5	14	1.3	0.31	0.78	36.3
Similar material	25.1	0.06	0.41	0.03	0.30	0.016	34.4
Bedrock	26.4	5.5	40.4	4.5	0.29	1.5	38
Similar material	25.4	0.11	0.88	0.08	0.31	0.029	35

Table 2 Composition and proportion (based on mass) similar materials for slipping mass and bedrock

Composition/%	Sand	Barite powder	Silicone oil	Vaseline	Water	Cement	Talc powder
Slipping mass	62	6	6	6	8	2	10
Bedrock	56	17	4	4	8	3	8

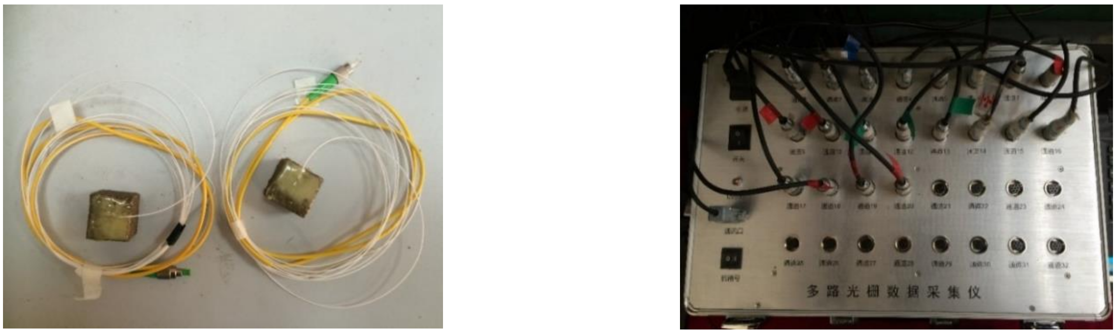

(a) (b)

Fig. 7 Strain monitoring system: (a) strain sensor of Fiber Bragg grating and (b) data acquisition system

the similar material compositions of slipping mass and bedrock are shown in Table 2.

3.3 Monitoring system

The stress and deformation of the slipping mass under loading are primary concerns and can provide direct cognition of progressive failure. Three measurement methods were adopted in this study, namely displacement measurement, strain measurement, and stress measurement in slipping mass and bedrock on the slope.

Strain sensing bars based on Fiber Bragg Grating (FBG) technology were used to measure the strain of the rock mass. The FBG strain test system features a small disturbance on the stress field of model rock, high measurement accuracy, continuous measurement, and strong anti-interference ability, which isn't easy to be disturbed by external factors, such as electromagnetic and temperature. The fiber strain bricks are 3 cm × 3 cm × 3 cm cubes made of similar materials, and fiber optics are pasted in the direction of 45° on the surface of bricks, as shown in Fig. 7(a). The monitoring data were acquired by the data acquisition system shown in Fig. 7(b).

The newly developed grating multi-point extensometer measurement system is adopted to measure the internal displacement of the rock mass. The measurement system is mainly composed of the following parts: the measuring point, casing, wire rope, positioning frame, grating ruler, a heavy hammer, signal conversion system, and data acquisition system. The grating ruler is the measuring element, including metrological grating and index grating, as shown in Fig. 8. The monitoring elements are convenient to embed in the rock mass and displacements can be displayed in real-time with high sensitivity.

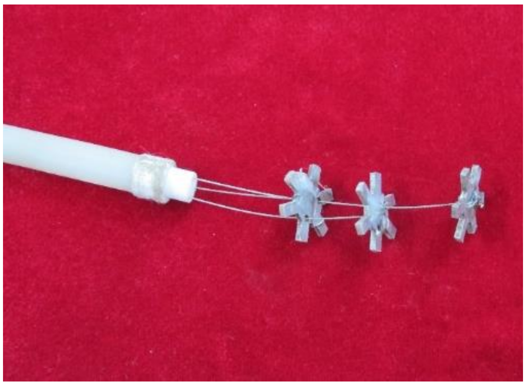

Fig. 8 Multi-point displacement meter

The stress of rock mass in slope was measured using a resistance type pressure cell, as shown in Fig. 9(a). The size of the pressure cell is $\Phi 17\times 7$ mm, and the measurement range is 0 ~ 1 MPa. The data acquisition system was shown in Fig. 9(b).

(a) (b)

Fig. 9 Stress monitoring system: (a) pressure cell of resistance type and (b) data acquisition system

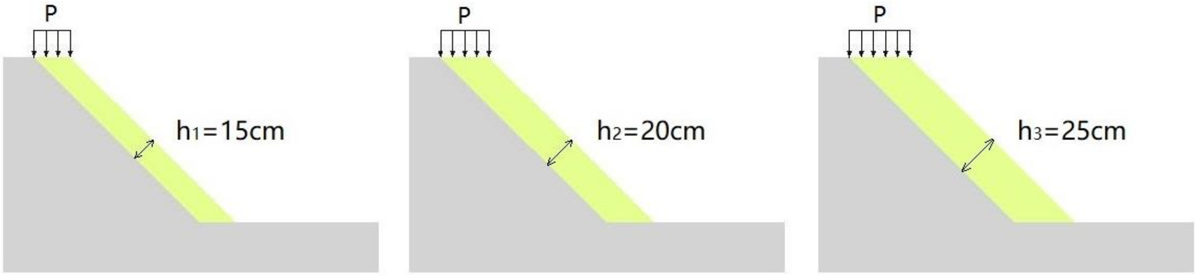

Fig. 10 Test models with different thicknesses of slipping mass, “P” means loading

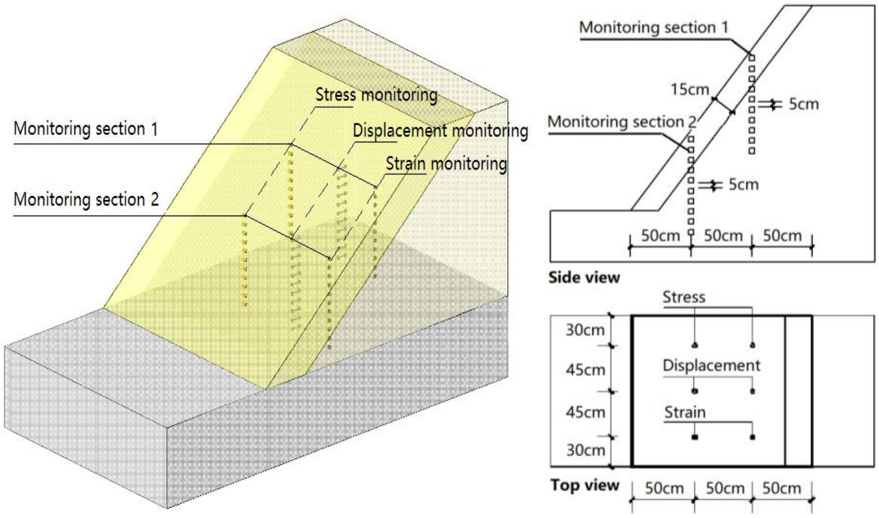

Fig. 11 Layout of monitoring scheme

3.4 Test program and monitoring scheme design

The tests conducted in this study were designed to examine stress, strain, and displacement of slope under loading, and then to study the mechanism of buckling failure. Also, the thickness of the slipping mass (“h” shown in Fig. 2) was set as 15 cm, 20 cm, and 25 cm to study the critical load of buckling failure corresponding to different thicknesses (h1, h2, h3), as shown in Fig. 10. Two monitoring sections were selected in the x-direction and displacement, strain, and stress of the rock mass were monitored in each section. The spacing between adjacent monitoring components of the same monitoring content is set as 5 cm. The monitoring scheme was shown in Fig. 11.

4. Test procedures

4.1 Model construction and embedding of monitoring components

The layering filling method was adopted for the construction of the model slope. Firstly, a similar material was developed according to the proportion and mixed well using a blender. After that, the material was placed on the base and compacted by a hammer so that it was dense in the test bench. Talcum powder was laid between the slipping mass and the bedrock to simulate the potential slip face. In this process, monitoring components were embedded based on the monitoring scheme design and data will be acquired

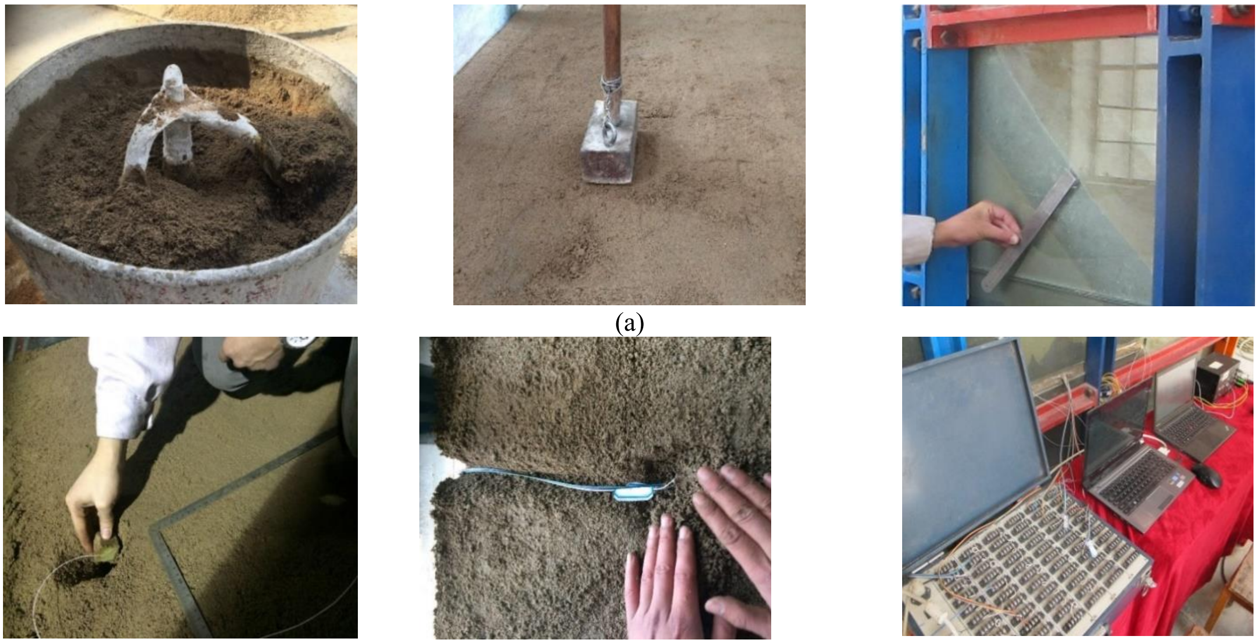
(a)

(b)

Fig. 12 (a) The model construction process and (b) the embedding process of monitoring components

(a) (b) (c)

Fig. 13 The loading system; (a) jack, (b) fuel injection pipes and (c) digital hydraulic auto-control system


Fig. 14 (a) The overall model test system in the loading process and (b) The typical failure in the loading process.

by the data acquisition system. The model construction is shown in Fig. 12(a), and the embedding process can be seen in Fig. 12(b).

4.2 Load application

In this test, the loading system includes jacks, fuel injection pipes, and a digital hydraulic auto-control system, as shown in Fig. 13. Each jack provides a 100 kN vertical load that was automatically controlled by a digital hydraulic system with a loading accuracy of 0.01 kN. Generally, the surface load, i.e., the pressure (Pa), is always used to describe the loading level. In our tests, the top surface areas of the slipping mass were different in different test models due to the thickness variation of the slipping mass, as shown in Fig. 10. Hence, the multi-step loading was adopted in the tests and the loading value of the latter step was 1 kN/m higher than the previous step, i.e., the stress increment is 5.1 kPa (h =15 cm), 3.8 kPa (h =20 cm) and 3.1 kPa (h =25 cm). The loading was terminated until the

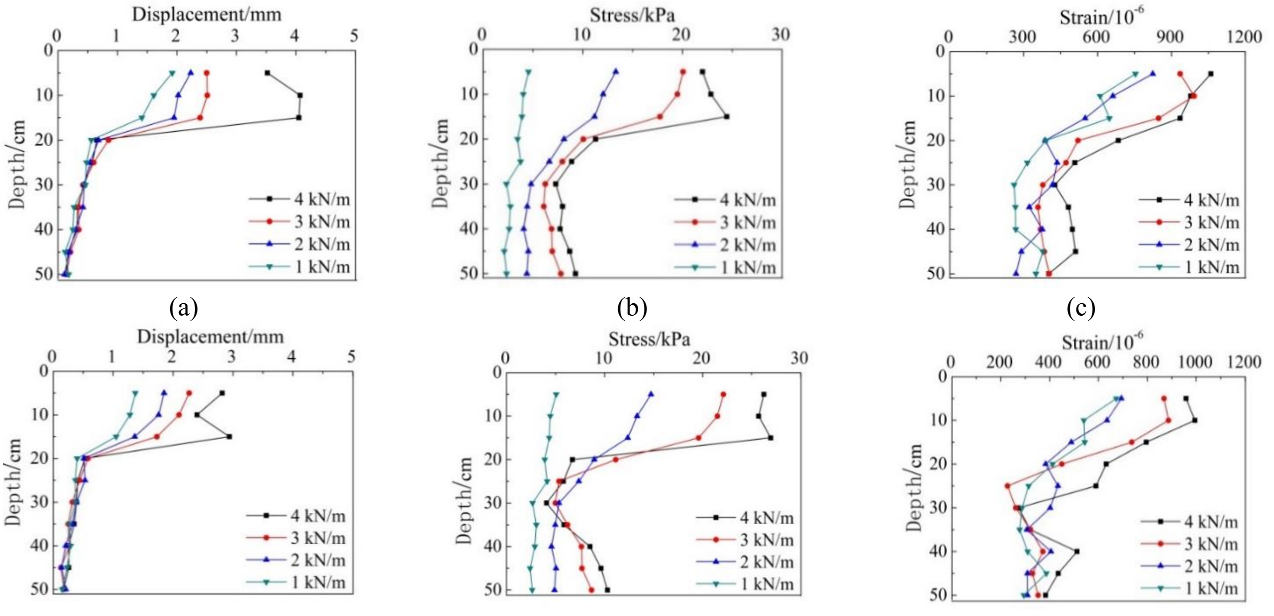

(d) (e) (f)

Fig. 15 Variation analysis of displacement, stress and strain in the test set where thickness of slipping mass is 15cm; (a), (b), (c) show the data of monitoring section 1 and (d), (e), (f) show the data of monitoring section 2. (1 kN/m ~ 5.1 kPa, 2 kN/m ~ 10.2 kPa, 3 kN/m ~ 15.3 kPa, 4 kN/m ~ 20.4 kPa)

slipping mass reached failure in each test condition, the failure was identified mainly based on the obvious cracks or buckling of the slipping mass. The monitoring data were measured in real-time under each loading and the displacement, stress, and strain of rock mass were analyzed when the data stabilized. The progression of buckling failure is monitored during the loading process to determine when the next loading should be carried out. The overall model test system in the loading process can be seen in Fig. 14(a) and the typical failure phenomenon was shown in Fig. 14(b).

5. Results analysis and discussion

The experimental phenomenon and variations of displacement, stress, and strain in rock mass of different test sets (h =15 cm, 20 cm, 25 cm) were analyzed in this section. The critical load of buckling failure was determined according to the monitoring data and experimental phenomenon. The load series are many when the thickness of the slipping mass increases. The representative monitoring data results were selected for drawing analysis to simplify the diagram.

When the thickness of slipping mass (h) is 15 cm, 4 kN/m (20.4 kPa) is the critical load on basis of the experimental phenomenon and monitoring data. We can see from Fig. 15 that the displacement, stress, and strain of slipping mass are larger than those of bedrock at the monitoring section 1 and 2. There are obvious data increase points on the curves and correspond to the slip face, which indicates that the slope is usually in relatively stable condition and the large change of mechanical properties happens in the shallow slipping mass under the top load. As shown in Figs. 15(a) and 15(d), when the load increases, the displacements of slipping mass significantly increase, whereas the variations of bedrock are not great. When the load increases to 4 kN/m (20.4 kPa), the displacement curves of monitoring section 2 show discontinuous variation, and the displacements in monitoring section 1 are significantly increased compared with the displacements monitoring data at the load level of 3 kN/m (15.3 kPa).

Stress monitoring data in Figs. 15(b) and 15(e) shows that the stress of slipping mass and bedrock both increase when the loading level changes from 1 kN/m (5.1 kPa) to 2 kN/m (10.2 kPa). However, the stress curve becomes a little different when the load continues to increase. The stress in the slipping mass still has an increasing trend, whereas the stress characteristic in the bedrock has normal stress characteristics caused by gravity. Under the top load, the slipping mass slides along the slip face and the stress in the bedrock increases due to the frictional traction. When the load increases, the bedrock close to the slip face has larger stress and variation amplitude. However, the buckling failure begins to occur when the load further increases. Some parts of the slipping mass break away from the slip face and frictional traction begins to decrease, which causes a decrease of stress in the bedrock close to the slip face. As shown in the graph, stresses monitored in monitoring section 2 are larger than that in section 1 and it shows the stress concentration occurs near the slope foot, similar to the findings of Pereira and Lana (2013). When the load increases to 4 kN/m (20.4 kPa), the stress regularity of the slipping mass is different from that under the previous load levels, which may be caused by cracking and failure in the slipping mass. This regularity can be considered as important evidence supporting that 4 kN/m (20.4 kPa) is the critical load causing buckling failure in this test set (h =15

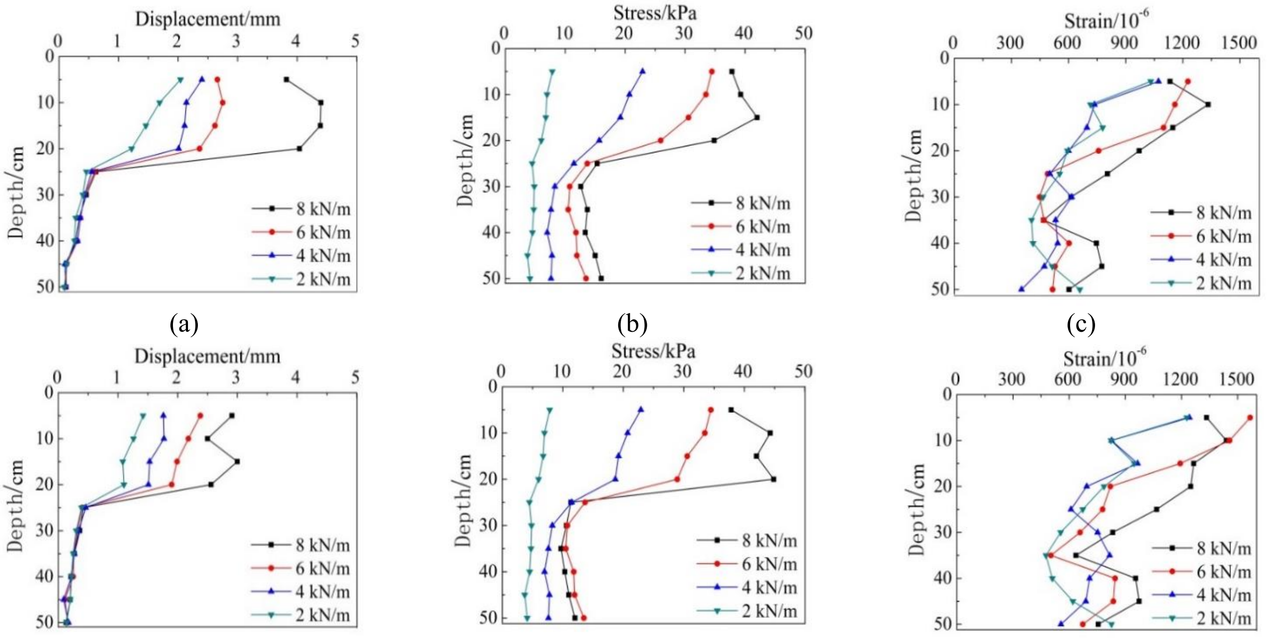

(a) (b) (c)

(d) (e) (f)

Fig. 16 Variation analysis of displacement, stress and strain in the test set where thickness of slipping mass is 20 cm; (a), (b), (c) show the data of monitoring section 1 and (d), (e), (f) show the data of monitoring section 2. (2 kN/m ~ 7.6 kPa, 4 kN/m ~ 15.2 kPa, 6 kN/m ~ 22.8 kPa, 8 kN/m ~ 30.4 kPa)

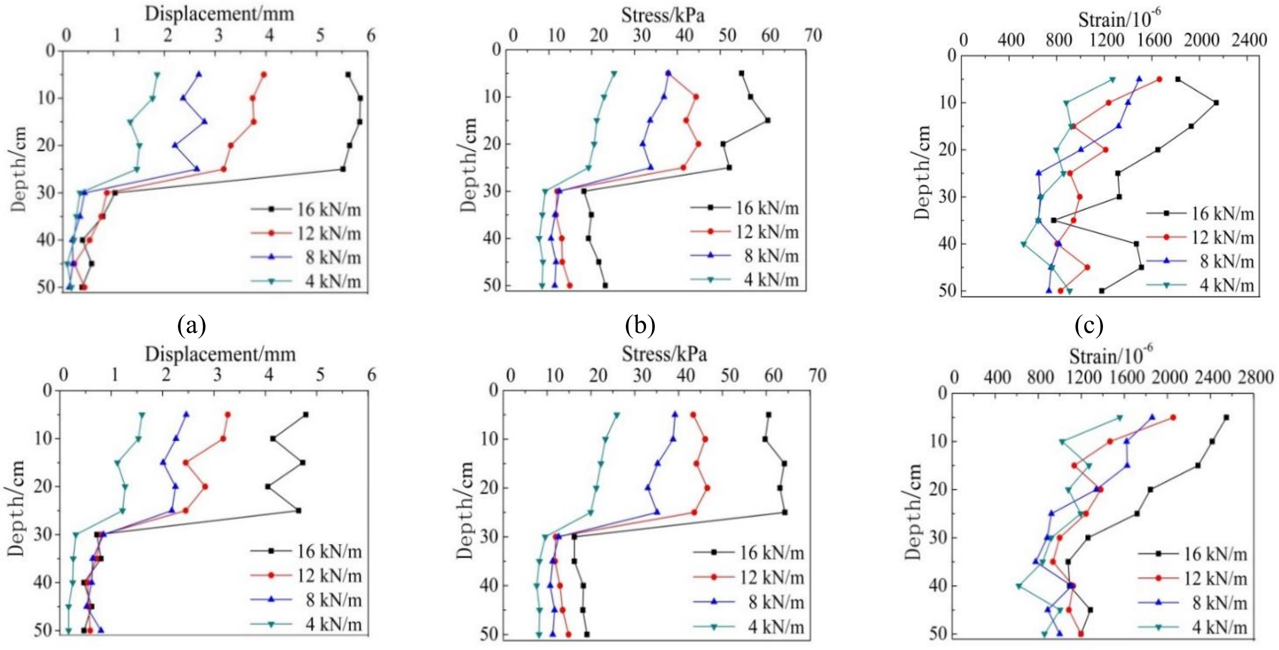

(a) (b) (c)

(d) (e) (f)

Fig. 17 Variation analysis of displacement, stress and strain in the test set where thickness of slipping mass is 25 cm; (a), (b), (c) show the data of monitoring section 1 and (d), (e), (f) show the data of monitoring section 2. (4 kN/m ~ 12.4 kPa, 8 kN/m ~ 24.8 kPa, 12 kN/m ~ 37.2 kPa, 16 kN/m ~ 49.6 kPa)

cm). It is also worth noting that the stress characteristics of the bedrock under the load of 3 kN/m (15.3 kPa) is an important predictor of buckling failure and can indicate that part of the slipping mass has separated from the slip face, compared with the displacement data that are later to some degree, as shown in Figs. 15(a), 15(b), 15(d), 15(e). Although the displacement is similar between the load conditions of 2 kN/m (10.2 kPa) and 3 kN/m (15.3 kPa), the stress evolution under the load condition of 3 kN/m (15.3 kPa) has been close to that under the critical load of 4 kN/m (20.4 kPa). When the sudden increases in displacement are captured, buckling failure may have occurred. This finding can give important guidance to the choice of monitoring and early warning schemes in actual slope engineering. From Fig. 15, it can be seen the displacement evolutions were similar among the four load conditions. However, the stress evolutions were different both in the slipping mass and the bedrock. In these cases, stress monitoring in bedrock is indispensable, and more than the slipping mass itself must be monitored.

The strain values of each measuring point in the slope are shown in Figs. 15(c) and 15(f). Strains in the bedrock close to the slip face have more evident variations with the increase in top load, especially when the load level is higher. In the loading process, the regularity of strain curves is not clear compared to the displacement and stress curves, which may be because the strain gauge is embedded in the slope by a prefabricated strain brick and it is difficult for it to fit well within the model body under loading. However, the uncoordinated deformation and increase of strain level in the slipping mass can also reflect the buckling failure combined with experimental phenomena while it may be difficult to evaluate the actual slope based on only strain data.

The monitoring data of test sets (h =20 cm, 25 cm) are shown in Figs. 16 and 17. The critical loads are considered as 8 kN/m (30.4 kPa) and 16 kN/m (49.6 kPa) for the two test sets, respectively, based on the monitoring data and experimental phenomena, which indicates that the sliding body can withstand a higher load level as the thickness of the slipping mass increases. The regularities of data curves are similar to the test set with h=15 cm and the displacement and stress are important predictors of buckling failure. Under the same loading level, the displacement and stress of the slipping mass at the same position decrease with the increase of the thickness of the slipping mass, while those of the bedrock are not influenced by the thickness of the slipping mass. The displacement of the slipping mass in Figs. 15(a) and 15(d) shows discontinuous deformation under a low load level. However, the stress, strain data, and experimental phenomena cannot reflect the buckling failure at that time, which indicates that the prediction of buckling failure in the slope should be based on multiple monitoring data.

Based on the comprehensive analysis of monitoring data of the three test sets, we observe that frictional resistance between the slipping mass and bedrock can withstand the load from the top surface together when under the low load level. With the increase of load level, the frictional resistance on the slip face cannot prevent the mass from sliding. The stress field and load-bearing ratio among the slipping mass, slip face, and bedrock are readjusted. At this time, there are larger deformations in the slipping mass and the stress in the bedrock is released to some degree because of the buckling deformation of the slipping mass, which causes evident data differences at the position close to the slip face. When the top load level reaches the critical load, buckling failure occurs and causes stress fluctuation in the slipping mass while the influence on stress in the bedrock is minimal. Aiming at the specific failure mechanism of buckling failure in the bedding slope, combining the previous references (Qi *et al*. 2015) and our test results, it can be analyzed that the main controlling factor of bedding slope instability is the potential slip face of the slope. Deformation often occurs first in the slip area of the upper slope. Due to the continuous action of external factors including top pressure, regional rock mass gravity, etc., the component force of slipping mass self-weight in the direction perpendicular to the slip face gradually decreases, causing creep deformation of the slipping mass along the slip face. The continuous deformation of the upper slipping mass will cause an extrusion effect on the lower part. The component force in the direction parallel to the slip face is the maximum force and the one in the direction perpendicular to the slip surface is the minimum force. Such a stress state causes tensile cracks that are parallel to the slip surface. However, the lower slipping mass' deformation parallel to the slip surface is hindered by the slope base, and the rock strata near the slope foot are uplifted or bent, accompanied by interlaminar tension crack, which eventually develops into the buckling failure of the slope. Comparison of data between monitoring sections 1 and 2, indicates that the displacement data in section 2 are less than that in section 1 because of the limit of the rock mass at slope foot and buckling deformation. Conversely, the stress data in section 2 are larger than in section 1 because of the self-weight and top load. Hence, the buckling failure usually occurs near the slope foot.

From the test results, the response of stress and displacement on buckling failure of the slope are later to some degree. Multiple information monitoring, analysis, and early warning technology are necessary for the prevention and control of engineering geological hazards. In addition to traditional displacement and stress monitoring methods, acoustic emission, infrared thermal imaging, and natural vibration frequency monitoring techniques are gradually being applied to the monitoring of engineering slope stability. (Salvoni and Dight 2016, Jiang *et al.* 2018, Toniuc and Pierron 2019). There is also a lot of research that should be conducted in this field.

6. Conclusions

In this paper, experiments were conducted on an independently developed comprehensive model test system to simulate slope buckling failure and the evolution process under exterior loading. The test system and test procedure were introduced in detail. During the loading process, the displacement, stress, and strain of slope were monitored and the change regularity of each parameter was analyzed to determine the critical load of buckling failure for different slipping mass thicknesses and to investigate the mechanism of this type of slope failure.

(1) A comprehensive model test bench considering landslide and rockfall experiments was specially developed as a test site and successfully applied to study slope buckling failure. In this test, new material was developed to simulate phyllite bedrock. The slope was artificial and the monitoring compositions were embedded in the rock mass according to a monitoring scheme. The experimental results show that the monitoring data can reflect the buckling

failure process and the overall test system is stable.

(2) A series of experiments were conducted to investigate the variation of displacement, stress, and strain as it relates to slipping masses of different thicknesses. Monitoring data and experimental phenomena show that displacement and stress are important predictors of buckling failure, especially the stress in the bedrock near the slip face that is usually ignored in the monitoring of an actual slope. However, the displacement data are varied later than the stress data. There were more fluctuations on stain curves compared to the other two parameters, which maybe because of the loading's influence on the coupling efficiency between the strain gauge and model body.

(3) The slipping mass with larger thickness has a larger critical load, and the critical stresses are 20.4 kPa, 30.4 kPa, and 49.6 kPa for the respective slipping mass thicknesses of 15 cm, 20 cm, and 25 cm. The bedrock was influenced less than the slipping mass and evident buckling deformation can be seen in the experiment. Based on the monitoring data and experimental phenomenon, the position near the slope foot is most prone to buckling failure.

Acknowledgments

The research was financially funded by the national key R&D program of China (2021YFB2301803, 2018YFB1600200), Science and Technology Project of Hebei Education Department (BJ2019050), Joint funds of NSFC (U2034207), Innovative Resarch Groups of Hebei province (E2021210099). Great appreciation goes to the editorial board and the reviewers of this paper.

References

Adhikary, D.P., Mühlhaus, H.B. and Dyskin, A.V. (2001), "A numerical study of flexural buckling of foliated rock slopes", *Int. J. Numer. Anal. Met.*, **25**, 871-884. https://doi.org/10.1002/nag.157.

Babanouri, N. and Sarfarazi, V. (2018), "Numerical analysis of a complex slope instability: Pseudo-wedge failure", *Geomech. Eng.*, **15**(1), 669-676. https://doi.org/10.12989/gae.2018.15.1.669.

Cavers, D.S. (1981), "Simple methods to analyze buckling of rock slopes", *Rock Mech. Rock Eng.*, **14**, 87-104. https://doi.org/10.1007/BF01239857.

Hu, J., Li, S., Li, L., Shi, S.S., Zhou, Z.Q., Liu, H.L. and He, P. (2018), "Field, experimental, and numerical investigation of a rockfall above a tunnel portal in southwestern China", *B. Eng. Geol. Environ.*, **77**, 1365-1382. https://doi.org/10.1007/s10064-017-1152-y.

Hu, J., Li, S., Liu, H., Li, L., Shi, S. and Qin, C. (2020), "New modified model for estimating the peak shear strength of rock mass containing nonconsecutive joint based on a simulated experiment", *Int. J. Geomech.*, **20**(7), 04020091. https://doi.org/10.1061/(ASCE)GM.1943-5622.0001732.

Jiang, T., Shen, Z.Z., Yang, M., Xu, L.Q., Gan, L. and Cui, X.B. (2018), "A new model approach to predict the unloading rock slope displacement behavior based on monitoring data", *Struct. Eng. Mech.*, **67**(2), 105-113. https://doi.org/10.12989/sem.2018.67.2.105.

Kim, J.M., Lee, S., Park, J.Y., Kihm, J.H. and Park, S. (2020), "A set of failure variables for analyzing stability of slopes and tunnels", *Geomech. Eng.*, **20**(3), 175-189. https://doi.org/10.12989/gae.2020.20.3.175.

Li, L., Hu, J., Li, S., Qin. C, Liu, H., Chen D. and Wang. J. (2021), "Development of a novel triaxial rock testing method based on biaxial test apparatus and its application", *Rock Mech. Rock Eng.* https://doi.org/10.1007/s00603-020-02329-3.

Lin, P., Liu, X., Zhou, W., Wang, R.K. and Wang, S.Y. (2015), "Cracking, stability and slope reinforcement analysis relating to the Jinping dam based on a geomechanical model test", *Arab. J. Geosci.*, **8**(7), 4393-4410. https://doi.org/10.1007/s12517-014-1529-1.

Moradi, G., Abdolmaleki, A. and Soltani, P. (2019), "Small-and large-scale analysis of bearing capacity and load-settlement behavior of rock-soil slopes reinforced with geogrid-box method", *Geomech. Eng.*, **18**(3), 315-328. https://doi.org/10.12989/gae.2019.18.3.315.

Nakajima, S., Abe, K., Shinoda, M., Nakamura, S., Nakamura, H. and Chigira, K. (2019), "Dynamic centrifuge model tests and material point method analysis of the impact force of a sliding soil mass caused by earthquake-induced slope failure", *Soils Found.* https://doi.org/10.1016/j.sandf.2019.08.004.

Ning, J.G., Liu, X.S., Tan, Y.L., Wang, J. and Tian, C.L. (2015), "Relationship of box counting of fractured rock mass with Hoek-Brown parameters using particle flow simulation", *Geomech. Eng.*, **9**(5), 619-629. https://doi.org/10.12989/gae.2015.9.5.619.

Pant, S.R. and Adhikary, D.P. (1999), "Implicit and explicit modelling of flexural buckling of foliated rock slopes", *Rock Mech. Rock Eng.*, **32**(2), 157-164. https://doi.org/10.1007/s006030050029.

Park, D.S. (2018), "Analyses of centrifuge modelling for artificially sensitive clay slopes", *Geomech. Eng.*, **16**(5), 513-525. https://doi.org/10.12989/gae.2018.16.5.513.

Pereira, L.C. and Lana, M.S. (2013), "Stress–strain analysis of buckling failure in phyllite slopes", *Geotech. Geol. Eng.*, **31**, 297-314. https://doi.org/10.1007/s10706-012-9556-8.

Qi, S., Lan, H. and Dong, J. (2015), "An analytical solution to slip buckling slope failure triggered by earthquake", *Eng. Geol.*, **194**, 4-11. https://doi.org/10.1016/j.enggeo.2014.06.004.

Salvoni, M. and Dight, P.M. (2016), "Rock damage assessment in a large unstable slope from microseismic monitoring-MMG Century mine (Queensland, Australia) case study", *Eng. Geol.*, **210**, 45-56. https://doi.org/10.1016/j.enggeo.2016.06.002.

Silva, C.H.C. and Lana, M.S (2014), "Numerical modeling of buckling failure in a mine slope", *Rem. Revista. Escola. De Minas.*, **67**(1), 81-86. https://doi.org/10.1590/S0370-44672014000100012.

Toniuc, H. and Pierron, F. (2019), "Infrared deflectometry for slope deformation measurements", *Exp. Mech.*, **59**(8), 1187-1202. https://doi.org/10.1007/s11340-019-00480-9.

Wang, S.H., Huang, R.Q. and Ni, P.P. (2017), "Advanced discretization of rock slope using block theory within the framework of discontinuous deformation analysis", *Geomech. Eng.*, **12**(4), 723-738. https://doi.org/10.12989/gae.2017.12.4.723.

Wang, X.T., Li, S.C., Xu, Z.H., Li, X.Z., Lin, P. and Lin, C.J. (2019) "An interval risk assessment method and management of water inflow and inrush in course of karst tunnel excavation", *Tunn. Undergr. Sp. Tech.*, **92**, 103033. https://doi.org/10.1016/j.tust.2019.103033.

Yamaguchi, K., Takeuchi, N. and Hamasaki, E. (2018), "Three-dimensional simplified slope stability analysis by hybrid-type penalty method", *Geomech. Eng.*, **15**(4), 947-955. https://doi.org/10.12989/gae.2018.15.4.947.

Zhang, B., Wang, H.X., Huang, J. and Xu, N.X. (2019), "Model test on slope deformation and failure caused by transition from open-pit to underground mining", *Geomech. Eng.*, **19**(2), 167-178. https://doi.org/10.12989/gae.2019.19.2.167.

Zhu, H.H., Yin, J.H., Dong, J.H. and Zhang, L. (2010), "Physical modelling of sliding failure of concrete gravity dam under overloading condition", *Geomech. Eng.*, **2**(2), 89-106. https://doi.org/10.12989/gae.2010.2.2.089.

GC